

ARTICLE

Open Access

# In situ-grown compressed NiCo<sub>2</sub>S<sub>4</sub> barrier layer for efficient and durable polysulfide entrapment

Shaozhan Huang<sup>1,2</sup>, Ye Wang<sup>1,3</sup>, Junping Hu<sup>1</sup>, Yew Von Lim<sup>1</sup>, Dezhi Kong<sup>1</sup>, Lu Guo<sup>1</sup>, Zongkui Kou<sup>4</sup>, Yaxin Chen<sup>5</sup> and Hui Ying Yang<sup>1</sup>

## Abstract

Modifying a polypropylene (PP) separator with a polysulfide barrier layer can improve the cycling performance of lithium–sulfur (Li–S) batteries. However, conventional slurry-coating- and vacuum-filtration-designed barriers usually show poor particle connection and require extra binder. Herein, we propose a facile in situ growth method and a subsequent compression strategy to design multifunctional NiCo<sub>2</sub>S<sub>4</sub> (NiCoS) nanosheet arrays on a PP membrane for high-performance Li–S batteries. The in situ grown NiCoS nanosheet arrays are interconnected, conductive and closely adhered to the PP membrane without using any binder. After mechanical compression treatment, the overall NiCoS film is compacted, lightweight (0.148 mg cm<sup>-2</sup>) and ultrathin (0.8 μm). Density functional theory calculations combined with adsorption and diffusion tests prove that the NiCoS nanosheets have highly efficient physical/chemical entrapping capabilities for preventing polysulfide shuttling. Moreover, in situ electrochemical impedance spectroscopy demonstrated that the NiCoS barrier could efficiently suppress polysulfide diffusion and concurrently facilitate redox reactions. When applying this multifunctional separator, a sulfur/carbon nanotube (S/CNT) cathode with high sulfur content (75 wt%) delivers significantly improved long-term cycling performance, with 0.056% capacity decay per cycle over 500 cycles. This work opens up new opportunities to design multifunctional separators by an in situ growth strategy for high-performance Li–S batteries.

## Introduction

With the ever-growing demands for higher energy density, conventional lithium-ion batteries (LIBs) can no longer satisfy applications in portable electronics and electric vehicles<sup>1–3</sup>. Lithium–sulfur (Li–S) batteries, which are inexpensive and environmentally benign and exhibit a high theoretical energy density of 2600 Wh kg<sup>-1</sup>, are considered one of the most promising candidates to meet the requirements of rapidly expanding electric vehicle markets<sup>4,5</sup>. However, the practical implementation of Li–S batteries is still impeded by their rapid capacity degradation, low Coulombic efficiency and short life span<sup>6,7</sup>. Specifically, the low electrical conductivity of S

and its discharge product (Li<sub>2</sub>S) leads to increased polarization and low sulfur utilization, and the dissolution of lithium polysulfide intermediates causes irreversible capacity loss and corrosion of Li-metal anode<sup>8</sup>.

To address these issues, tremendous efforts have been devoted to the development of porous cathode host materials to immobilize polysulfides by confining sulfur in porous carriers, such as porous carbon materials<sup>9,10</sup>, heteroatom-doped carbon/graphene materials<sup>11</sup>, and polar inorganic materials<sup>12,13</sup>. These efforts have significantly enhanced sulfur utilization and improved the performance of Li–S batteries. However, in most cases, host material contents as high as 30–60 wt% are needed to encapsulate the polysulfides and suppress their shuttling, which sacrifices a large proportion of energy density (20–50%) of the whole cell in contrast to the sulfur/carbon black cathode with 70 wt% sulfur<sup>14</sup>. Therefore, it is desirable to fabricate Li–S batteries with both a high sulfur content and a stable cycling performance.

Correspondence: Hui Ying Yang (yanghuiying@sutd.edu.sg)

<sup>1</sup>Pillar of Engineering Product Development, Singapore University of Technology and Design, 8 Somapah Road, 487372 Singapore, Singapore

<sup>2</sup>Hubei Key Laboratory of Catalysis and Materials Science, South-Central University for Nationalities, Wuhan, Hubei 430074, China

Full list of author information is available at the end of the article.

© The Author(s) 2019



**Open Access** This article is licensed under a Creative Commons Attribution 4.0 International License, which permits use, sharing, adaptation, distribution and reproduction in any medium or format, as long as you give appropriate credit to the original author(s) and the source, provide a link to the Creative Commons license, and indicate if changes were made. The images or other third party material in this article are included in the article's Creative Commons license, unless indicated otherwise in a credit line to the material. If material is not included in the article's Creative Commons license and your intended use is not permitted by statutory regulation or exceeds the permitted use, you will need to obtain permission directly from the copyright holder. To view a copy of this license, visit <http://creativecommons.org/licenses/by/4.0/>.

In this regard, introducing a separator with a functional barrier layer on the cathode side of a commercial polypropylene (PP) membrane is an effective strategy to inhibit the migration of polysulfides from cathodes to anodes, which could improve the cycling stability and concurrently enable high sulfur contents due to the reduced utilization of host materials<sup>15</sup>. Currently, various nanomaterials, such as porous carbon-based materials, graphene/graphene oxides, metal oxides/sulfides and metal-organic frameworks, have been employed as barrier layers to suppress shuttling of polysulfides to the anodes<sup>14,16–19</sup>. Although potential successes have been achieved, some issues still exist in this battery system. First, most of the functional separators are fabricated through slurry-coating and vacuum-filtration methods, which need extra binder or additives<sup>15,20</sup>. Second, these postcoating processes usually induce poor particle connection and arrangement of the nanomaterials, leading to unstable structures and discontinuous electron pathways. In addition, the slurry-coated barrier layers are usually thick and have a high weight density (usually  $>0.3 \text{ mg cm}^{-2}$ ), leading to reduced sulfur contents as well as low volumetric/gravimetric energy densities. Therefore, it is highly desirable to develop an effective approach to fabricate a novel binder-free barrier layer with a percolated electron pathway, as well as thin and lightweight characteristics with high polysulfidetrapping capabilities.

Herein, we propose a simple in situ growth and subsequent compression strategy to grow a compressed  $\text{NiCo}_2\text{S}_4$  (NiCoS) nanosheet array film on a commercial PP separator (NiCoS/PP-P) for high-performance Li–S batteries. The rational design of this novel separator is based on the following considerations: (i) The novel porous NiCoS nanosheet arrays are interconnected and electrically conductive<sup>21,22</sup>, facilitating lithium-ion diffusion and providing continuous electron transport pathways. (ii) The in situ-grown NiCoS thin film is strongly adhered to the PP separator without using any binder. (iii) The areal mass and thickness of the compressed NiCoS nanosheet arrays grown on the PP separator are only  $0.148 \text{ mg cm}^{-2}$  and  $0.8 \text{ }\mu\text{m}$ , leading to high sulfur contents throughout the whole cell. (iv) The mechanical compression treatment leads to a dense NiCoS thin film, which can block the polysulfide diffusion pathway. (v) The polar NiCoS nanosheet arrays can provide strong chemical adsorption toward polysulfides. (vi) The compressed NiCoS barrier layer can enable formation of a commercially available CNT/S cathode with a high sulfur content (up to 75 wt%), which is appealing for practical applications. As a result, the compressed NiCoS barrier layer efficiently suppresses polysulfide shuttling between the cathode and anode, resulting in a significantly improved Coulombic efficiency of 99.6%, high areal capacity of  $2.63 \text{ mAh cm}^{-2}$  (0.5 C) and cycling

performance with only 0.056% capacity decay per cycle over 500 cycles at 0.5 C.

## Materials and methods

### Synthesis of a NiCoS/PP-P separator

First, 1 mol  $\text{Ni}(\text{NO}_3)_2 \cdot 6\text{H}_2\text{O}$ , 2 mol  $\text{Co}(\text{NO}_3)_2 \cdot 6\text{H}_2\text{O}$  and 10 mol hexamethylenetetramine ( $\text{C}_6\text{H}_{12}\text{N}_4$ ) were dissolved in a 70 mL solution containing distilled water/ethanol (v/v, 1:1). Then, a piece of commercial polypropylene (PP, Celgard 2400) bound on a glass slide was immersed into the abovementioned solution and aged for 30 min. Afterward, the PP/glass slide and solution were transferred into a sealed container (100 ml) and held at  $90^\circ\text{C}$  for 8 h. After reaction, the NiCo-layered double hydroxide (NiCo-LDH) grew on the PP membrane. Then, the NiCo-LDH/PP/glass slide was removed and rinsed with distilled water and ethanol several times. Next, the NiCo-LDH/PP/glass slide was transferred into a sealed container (100 ml) filled with a 70 mL  $\text{Na}_2\text{S}$  solution (20 mM) and kept at  $110^\circ\text{C}$  for 6 h. Then, the NiCoS/PP membrane was collected, washed with distilled water and dried at  $60^\circ\text{C}$  in a vacuum oven. Finally, the NiCoS/PP membrane was sandwiched between two Al foils (each with a thickness of  $15 \text{ }\mu\text{m}$ ) and compressed by a vertical electric calender machine (MSK-2150, Shenzhen Kejing Star Technology) with a roller distance of  $80 \text{ }\mu\text{m}$ . After compression, the NiCoS/PP-P membrane was obtained. During the sulfurization process, the nanosheet arrays adsorbed on the glass were peeled off owing to the weak interaction between NiCoS and glass. Then, the free-standing NiCoS nanosheet arrays were collected from the solution. To obtain nickel sulfide, nickel-manganese sulfide and cobalt-manganese sulfide thin films, the corresponding metal nitrates were used in the reaction.

### Adsorption and diffusion test

For the adsorption test,  $\text{Li}_2\text{S}$  and sulfur with a molar ratio of 1:5 were added into a mixed 1,2-dimethoxyethane and 1,3-dioxolane (DOL/DME) solution (1:1, v/v) and stirred overnight at  $60^\circ\text{C}$ . The concentration of  $\text{Li}_2\text{S}_6$  in the solution was  $3 \text{ mmol L}^{-1}$ . Then, 10 mg of NiCoS nanosheet arrays were added to 3 mL of the abovementioned  $\text{Li}_2\text{S}_6$  solution. The mixture was stirred and rested for 3 h for observation. For the diffusion test, H-shaped glass bottles were used. A 5 mL DME solution containing  $0.1 \text{ mol L}^{-1}$   $\text{Li}_2\text{S}_6$  was added to the left bottle, and 5 mL pure DME was added to the right bottle. The separators were sandwiched between two bottles. The H-shaped glass bottles were placed in an Ar-filled glove box for observation.

### Materials characterizations

The crystal structure of the NiCoS nanosheet arrays was determined by a Bruker D8 advance X-ray diffractometer

(Cu K $\alpha$ ,  $\lambda = 0.154$  nm, 40 kV, 25 mA). In situ XRD measurements were performed in a stainless-steel Swagelok-type cell, which was connected to a multichannel battery testing system (Neware, China). Field-emission scanning electron microscopy was performed on a JEOL JSM-7600F microscope equipped with a field-emission gun at a 10 kV acceleration voltage. Transmission electron microscopy (TEM) was performed on a JEOL JEM-2100F microscope operating at 200 kV acceleration voltage. N<sub>2</sub> adsorption/desorption isotherms were measured on an automated gas sorption analyzer (Autolab-iQ, Quantachrome Instruments). The surface area was determined by a multipoint Brunauer–Emmett–Teller (BET) method. X-ray photoelectron spectroscopy (XPS, PHI 5600) was used to analyze the surface electronic states by using monochromatic Al K $\alpha$  X-rays (350 W) and a pass energy of 30 eV.

### Electrochemical measurements

The commercial sulfur and carbon nanotubes in a weight ratio of 75:25 were mixed and heated at 155 °C in a sealed bottle. Then, the obtained CNT/S composite was mixed with PVDF at a weight ratio of 90:10 to form the cathode slurry. Then, the slurry was coated onto the Al foil and dried at 60 °C for 12 h in a vacuum oven. The areal sulfur loading of the electrode is  $\sim 1.5$ – $2$  mg cm<sup>-2</sup>. For comparison, thicker CNT/S electrodes with higher sulfur loading values of 3.4 and 5.3 mg cm<sup>-2</sup> were also prepared. The electrolyte/sulfur ratio of all electrodes was 10  $\mu$ L mg<sup>-1</sup>. Lithium foil was employed as the anode, and bare PP, NiCoS/PP, and NiCoS/PP-P were used as the separators. The electrolyte was 1 M bis(trifluoroethanesulfonyl) imide lithium (LiTFSI) in DME/DOL (v/v = 1:1) containing 0.3 M LiNO<sub>3</sub>. CV measurements were carried out by an electrochemical workstation (VMP3, Bio-Logic, Claix, France) at different scan rates. In situ electrochemical impedance spectra (EIS) were measured with the same electrochemical workstation in the 100 kHz–10 mHz frequency range with 10 mV of AC amplitude at different potentials. Galvanostatic discharge/charge cycling was studied in a potential range of 1.7–2.8 V, using a multichannel battery testing system (Neware, Shenzhen, China).

### Density functional theory calculations

All the calculations are based on density functional theory (DFT) using the plane-wave pseudopotentials with the Perdew–Burke–Ernzerhof (PBE) exchange–correlation functional as implemented in the Vienna Ab initio Simulation Package (VASP)<sup>23,24</sup>. The effective onsite Coulomb interaction values used here are taken from the literature: 6.4 eV for Ni and 4.0 eV for Co<sup>25</sup>, with  $J = 1$  eV for both. A cutoff energy of 500 eV is employed for the plane-wave expansion of the wave functions. The Brillouin zone is sampled with a  $3 \times 5 \times 1$  Monkhorst–Pack  $k$ -point mesh<sup>26</sup>

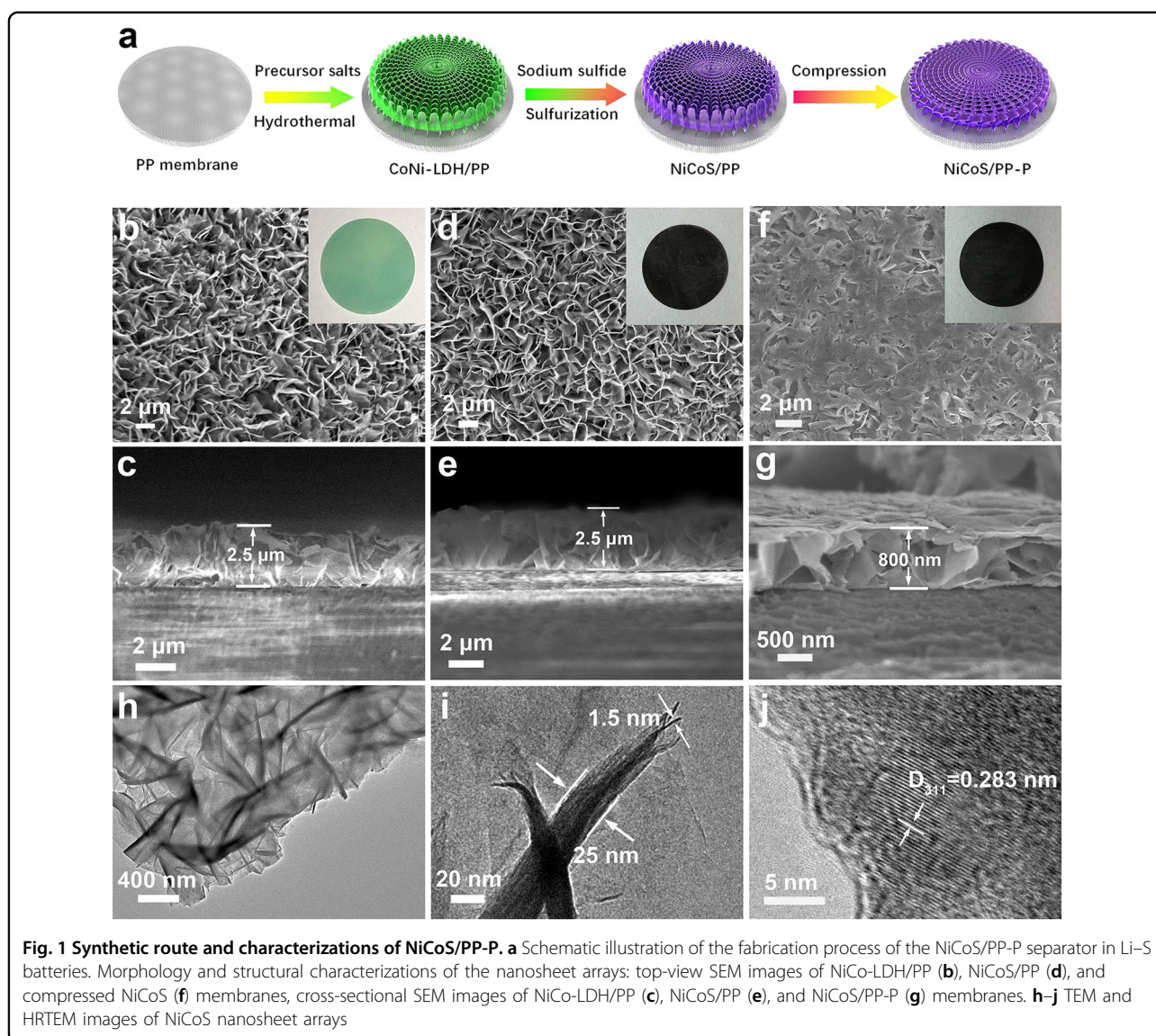
for structural optimization. The convergence criteria for the total energy and ionic forces were set to  $10^{-4}$  eV and 0.01 eV/Å, respectively. The construction with a 20 Å vacuum zone in the  $z$  direction minimizes the interactions between adjacent images.

### Results

The entire fabrication procedure to generate the compressed NiCoS/PP membrane is schematically shown in Fig. 1a (see details in the Materials and methods section). First, a thin layer of Ni–Co layered double hydroxide (LDH) nanosheet arrays was grown onto the PP membrane through a facile hydrothermal reaction at a low temperature of 90 °C. As revealed in Fig. S1a, b, after the reaction, the PP membrane was uniformly covered with a green NiCo-LDH layer without any crack. The presence of functional groups (e.g., methyl groups) in PP may assist in the capture of LDH crystal seeds on the PP membrane, which improves the adherence and mechanical stability of the thin film compared with the standard solution and colloidal deposition techniques such as spin coating, dip coating, vacuum filtration, and doctor blading<sup>27</sup>. Second, the obtained NiCo-LDH/PP membrane was chemically transformed to NiCoS/PP after a solution sulfurization reaction (Fig. S1a). Finally, the compressed NiCoS/PP was obtained after a rational mechanical compression treatment of the NiCoS/PP, which is denoted as NiCoS/PP-P. The chemical growth and physical compression processes result in excellent adhesion of the NiCoS thin film onto the PP membranes, as confirmed by the folding/unfolding test (Fig. S1c). Over the entire process, the PP membrane preserves the porous structure owing to its high thermal and chemical stability, as revealed by the SEM images (Fig. S2).

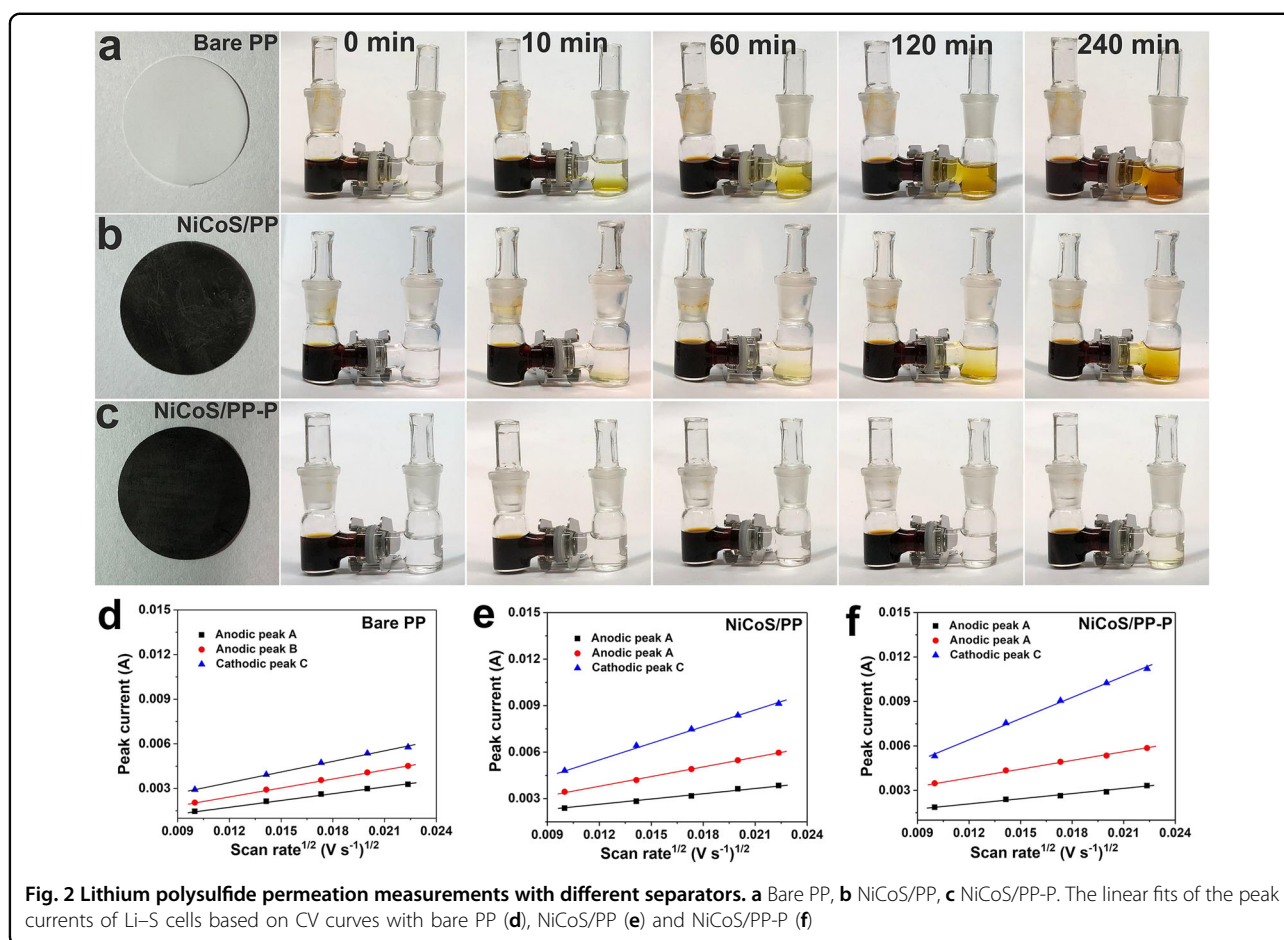
Scanning electron microscopy (SEM) images of several membranes are shown in Fig. 1b–g. The uniform green layer coverage indicates that the NiCo-LDH thin film is continuously and uniformly grown on the membrane (inset in Fig. 1b). The SEM image reveals that the NiCo-LDH consists of interconnected porous nanosheet arrays with a thickness of  $\sim 2.5$   $\mu$ m (Fig. 1b, c). After sulfurization, the NiCo-LDH thin film is converted to a NiCoS thin film (Fig. S3a, NiCo<sub>2</sub>S<sub>4</sub>, JCPDS No. 01-073-1704). The obtained NiCoS thin film retains the initial 3D porous nanosheet array structure (Fig. 1d) with an average thickness of 2.5  $\mu$ m (Fig. 1e). A high-magnification SEM image reveals that the thickness of the NiCoS nanosheet is  $\sim 25$  nm (Fig. S3b). According to the calculation, the loading density of the NiCoS thin film on the PP membrane is  $\sim 0.148$  mg cm<sup>-2</sup>. Interestingly, during the sulfurization process, some freestanding NiCoS nanosheet arrays can be collected from the solution (see the details in the Materials and methods section). The SEM images reveal that the NiCoS nanosheet array has two different





sides: the top side that is exposed to the solution and the bottom side that is in contacts with the substrate (Fig. S4). The top side (Fig. S4c) presents the same nanosheet array morphology as that observed in Fig. 1d, while the bottom side shows much denser and smaller nanosheets with abundant mesopores (Fig. S4d), which is beneficial for the suppression of polysulfide shuttling. The corresponding elemental mapping images demonstrate the uniform distribution of S, Co and Ni in the NiCoS nanosheet arrays (Fig. S5). The nitrogen adsorption-desorption isotherm of NiCoS nanosheet arrays exhibit a typical type IV isotherm with remarkable H3 hysteresis (Fig. S6a)<sup>28</sup>, validating a mesoporous structure with a high BET surface area of  $61.3 \text{ m}^2 \text{ g}^{-1}$ . The microstructure of the NiCoS nanosheet array was characterized by transmission electron microscopy (TEM), as depicted in Fig. 1h–j. The low-

magnification TEM image (Fig. 1h) indicates that the nanosheet array is porous and interconnected. A high-magnification TEM image (Fig. 1i) confirms that the thickness of the nanosheet is  $\sim 25 \text{ nm}$ , consistent with the SEM image. Notably, the thick nanosheet (25 nm) is composed of many thinner nanosheets with a thickness of  $\sim 2.5 \text{ nm}$ , which creates abundant nanopores within the thick nanosheets. A high-resolution TEM (HRTEM) image shows well-resolved lattice fringes with spacings of  $0.283 \text{ nm}$ , corresponding to the (311) plane of cubic  $\text{NiCo}_2\text{S}_4$  (Fig. 1j). The hierarchical porous structure and ultrathin nanosheets can facilitate fast  $\text{Li}^+$  diffusion and provide abundant chemical anchoring sites for polysulfides in subsequent electrochemical tests. However, owing to the large pores within the NiCoS nanosheet arrays, the polysulfides are likely to eventually migrate



into the anode side, leading to the shuttling effect. Thus, to improve the ability of this physical layer to suppress polysulfide diffusion, the NiCoS/PP membrane was compressed by a twin-roller machine (see the details in the Materials and methods section). After compression treatment, the NiCoS thin film remained intact without any break (inset in Fig. 1e), indicating the robust adhesion of the NiCoS thin film onto the PP membrane. The SEM image shows that the top part of the nanosheets becomes bent and uniformly covers the middle/bottom parts of the NiCoS nanosheets (Fig. 1e). The cross-section SEM image reveals that the thickness of the NiCoS thin film is reduced to 800 nm (Fig. 1f), which is much smaller than that of the as-prepared NiCoS nanosheet arrays ( $\sim 2.5 \mu\text{m}$ ). Moreover, several layers of NiCoS nanosheets cover the middle/bottom parts of the NiCoS thin film (Fig. S7). The areal mass loading of the compressed NiCoS remains at  $\sim 0.148 \text{ mg cm}^{-2}$ . The thickness and areal mass loading are lower than those of many reported previously (see the comparison in Table S1), such as the graphene nanosheets<sup>29</sup> ( $1.3 \text{ mg cm}^{-2}$ , thickness of  $30 \mu\text{m}$ ) via the slurry-coating method and  $\text{Ti}_3\text{C}_2$  MXene<sup>30</sup> ( $0.4 \text{ mg cm}^{-2}$ , thickness of  $2 \mu\text{m}$ ) via the vacuum-filtration method.

More importantly, the in situ growth strategy can be broadened to fabricate other functional separators, such as nickel sulfide/PP, nickel-manganese sulfide/PP, cobalt-manganese sulfide/PP, as shown in Fig. S8. Notably, the compressed NiCoS/PP membrane shows a smaller BET surface area of  $36.6 \text{ m}^2 \text{ g}^{-1}$  than the uncompressed NiCoS/PP membrane ( $42.8 \text{ m}^2 \text{ g}^{-1}$ , Fig. S6c, d).

To prove the advantage of this thin film in suppressing polysulfide migration, the permeability of polysulfide through several separators was examined, as shown in Fig. 2. H-shaped glass bottles were used for this examination, where the separator was sandwiched between the two bottles. The left bottle is filled with 1,2-dimethoxyethane (DME) solution containing 0.1 M  $\text{Li}_2\text{S}_6$ , and the right bottle is filled with pure DME solvent. Over time,  $\text{Li}_2\text{S}_6$  diffusion to the pure DME can be clearly observed with different separators. For bare PP, the  $\text{Li}_2\text{S}_6$  diffuses to the right bottle rapidly after only 10 min, indicating the poor capability of the bare porous PP to block the polysulfides (Fig. 2a). After introducing the NiCoS layer, the NiCoS/PP shows much less polysulfide diffusion, suggesting that the NiCoS layer can chemically/physically trap the polysulfides (Fig. 2b). However, the porous NiCoS layer



cannot suppress the polysulfide diffusion effectively since a large amount of  $\text{Li}_2\text{S}_6$  migrates to the pure DME across the NiCoS/PP membrane after 240 min. In contrast, the NiCoS/PP-P with compression demonstrates the significant improvement in trapping the polysulfides (Fig. 2c). Even after 240 min, the polysulfide migration phenomenon is still negligible, revealing the superior polysulfide blocking capability of the compressed NiCoS thin film. The polysulfide permeability test implies that the NiCoS/PP-P separator has a strong application potential in Li–S batteries.

To explore whether the introduction of NiCoS thin film will influence the  $\text{Li}^+$  diffusion coefficient, a series of cyclic voltammograms (CVs) combined with the linear fits of peak currents were obtained for the cells with bare PP, NiCoS/PP and NiCoS/PP-P (Fig. S9, Fig. 2d–f). The  $\text{Li}^+$  diffusion coefficients ( $D_{\text{Li}^+}$ ) were calculated based on the Randles–Sevcik equation<sup>31</sup>.

$$I_p = 2.69 \times 10^5 n^{1.5} A D_{\text{Li}^+}^{0.5} C_{\text{Li}} \nu^{0.5} \quad (1)$$

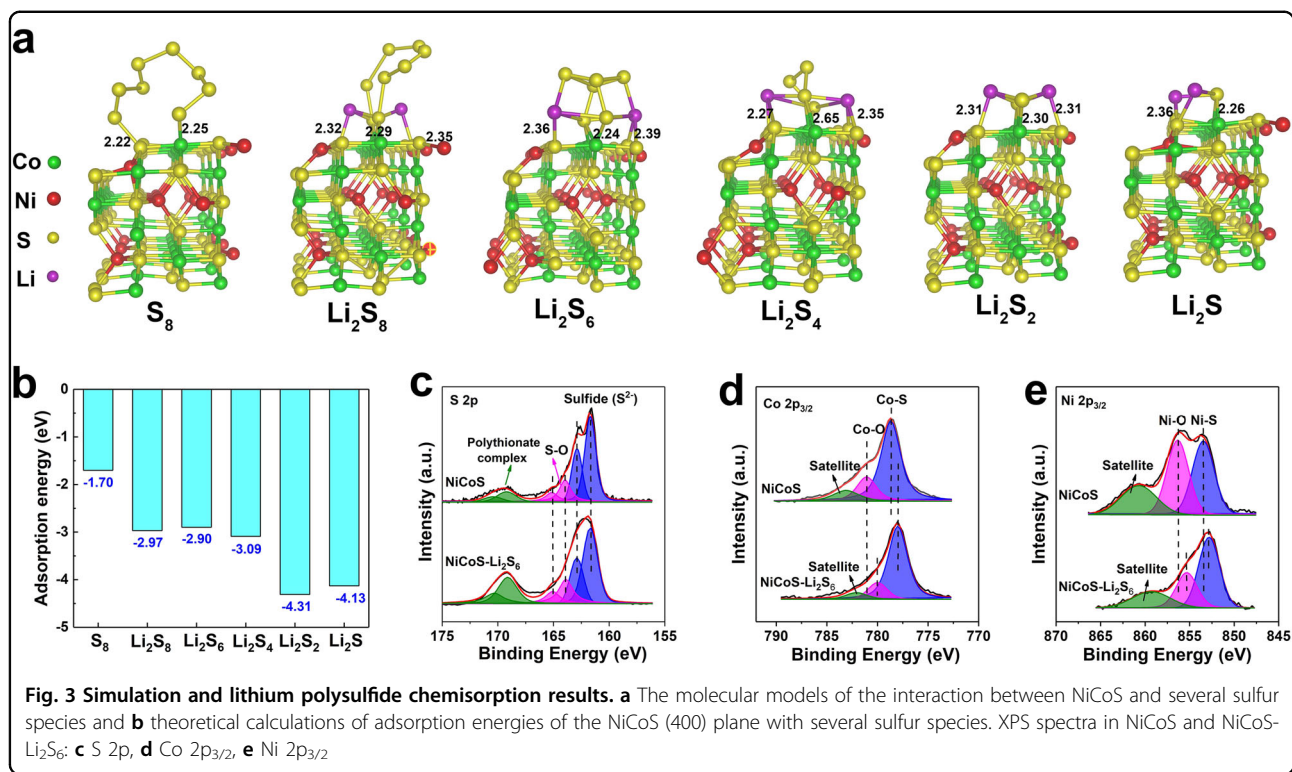
where  $D_{\text{Li}^+}$  represents the lithium diffusion coefficient ( $\text{cm}^2 \text{s}^{-1}$ ),  $I_p$  is the peak current (A),  $n$  is the number of electrons involved in the reaction ( $n = 2$  for Li–S battery),  $A$  is the area of the electrode,  $C_{\text{Li}}$  is the concentration of  $\text{Li}^+$  in the reaction ( $\text{mol L}^{-1}$ ) and  $\nu$  refers to the scan rate ( $\text{V s}^{-1}$ ). It is noted that the  $D_{\text{Li}^+}$  of NiCoS/PP ( $3.00 \times 10^{-9}$ ) and NiCoS/PP-P ( $3.00 \times 10^{-9}$ ) at peak A is slightly smaller than that of bare PP ( $4.65 \times 10^{-9}$ ), indicating that the introduction of the NiCoS layer will slow the  $\text{Li}^+$  diffusion across the separator at an early stage (Table 1). However, at peak B, the  $D_{\text{Li}^+}$  of NiCoS/PP ( $8.94 \times 10^{-9}$ ) and NiCoS/PP-P ( $8.75 \times 10^{-9}$ ) become slightly larger than that of bare PP ( $8.49 \times 10^{-9}$ ). Generally, at peak B, the solid lithium sulfides are likely to deposit at the cathode-separator interface as an insulating layer and hinder  $\text{Li}^+$  diffusion<sup>32</sup>. The porous NiCoS nanosheet arrays in this work can provide abundant voids to accommodate various redox species and suppress the insulating layer formation, resulting in enhanced lithium-ion diffusion<sup>14</sup>. Remarkably, at peak C, the bare PP exhibits much smaller  $D_{\text{Li}^+}$  ( $1.15 \times 10^{-8}$ ) than the NiCoS/PP ( $2.64 \times 10^{-8}$ ) and NiCoS/PP-P ( $4.89 \times 10^{-8}$ ), indicating that the polysulfide shuttling to the anode results in debilitated  $\text{Li}^+$  diffusion

during the subsequent anodic process owing to the corrosion of the anode and increased viscosity of the anolyte. Therefore, the introduction of the NiCoS layer nearly has no notable degradation on  $\text{Li}^+$  diffusion. To further illustrate the superiority of the NiCoS barrier layer, the self-discharge phenomenon is investigated by monitoring the open circuit voltage (OCV) of Li–S cells with different separators. As shown in Fig. S10a, the PP membrane with the NiCoS layer delivers higher initial OCV (2.58 V and 2.6 V for NiCoS and compressed NiCoS, respectively) than the bare PP (2.39 V). After several hours, the OCV of NiCoS quickly decreases to 2.45 V, while the compressed NiCoS maintains a high OCV value of 2.58 V, suggesting that the compressed NiCoS thin film on the PP membrane can effectively depress the self-discharge phenomenon.

As mentioned above, the NiCoS thin film can not only serve as a physical layer to suppress the polysulfide diffusion to the anode but also provide abundant chemical bonding sites to trap the polysulfide species. Density functional theory (DFT) calculations were conducted to evaluate the adsorption energies of NiCoS to polysulfides. As shown in Fig. 3a, b, the (400) surface of NiCoS renders high adsorption energies of  $-1.7$ ,  $-2.97$ ,  $-2.90$ ,  $-3.09$ ,  $-4.31$ , and  $-4.13$  eV for  $\text{S}_8$ ,  $\text{Li}_2\text{S}_8$ ,  $\text{Li}_2\text{S}_6$ ,  $\text{Li}_2\text{S}_4$ ,  $\text{Li}_2\text{S}_2$ , and  $\text{Li}_2\text{S}$  species, respectively, suggesting the strong chemical anchoring of polysulfides onto the NiCoS nanosheets. A polysulfide adsorption test was carried out to further demonstrate the strong adsorption of NiCoS nanosheets to polysulfides. After mixing the NiCoS nanosheet arrays with  $3 \text{ mmol L}^{-1}$   $\text{Li}_2\text{S}_6$  solution, the  $\text{Li}_2\text{S}_6$  solution shows rapid discoloration within 3 h, indicating the strong chemical interaction between NiCoS and polysulfides (Fig. S10b). The chemical adsorption mainly originates from several interactions: chemical bonding between S atoms (in  $\text{Li}_2\text{S}_6$ ) and Co/Ni and chemical bonding between Li and S (in NiCoS). To better clarify the chemical interaction between NiCoS and polysulfides, X-ray photoelectron spectroscopy (XPS) was performed (Fig. 3c–e). In the S 2p spectrum, the pristine NiCoS presents two major S 2p<sub>3/2</sub> peaks: 161.7 and 164.0 eV (Fig. 3c). The former corresponds to  $\text{S}^{2-}$ , and the latter belongs to S–O that results from superficial oxidation. After intercalation with  $\text{Li}_2\text{S}_6$ , the intensities of the  $\text{S}^{2-}$  and S–O peaks significantly decrease. Furthermore, the S 2p<sub>3/2</sub> peaks at 169.1 eV become stronger. This peak is assigned to a polythionate complex, which comes from the chemical reaction between long-chain polysulfide and NiCoS<sup>33</sup>. The polythionate complex in the electrode is proven to be reversible and can serve as an anchor and transfer mediator to inhibit active materials (polysulfides) dissolution into the electrolyte<sup>34</sup>. The oxidation of  $\text{Li}_2\text{S}_6$  to a polythionate complex is accompanied by a valence state decrease of Co and Ni, as identified in Fig. 3d, e. In the

**Table 1** The Li-ion diffusion coefficient with different separators

Samples	Bare PP	NiCoS/PP	NiCoS/PP-P
$D_{\text{Li}^+}$ at peak A ( $\text{cm}^2 \text{s}^{-1}$ )	$4.65 \times 10^{-9}$	$3.00 \times 10^{-9}$	$3.00 \times 10^{-9}$
$D_{\text{Li}^+}$ at peak B ( $\text{cm}^2 \text{s}^{-1}$ )	$8.49 \times 10^{-9}$	$8.94 \times 10^{-9}$	$8.75 \times 10^{-9}$
$D_{\text{Li}^+}$ at peak C ( $\text{cm}^2 \text{s}^{-1}$ )	$1.15 \times 10^{-8}$	$2.64 \times 10^{-8}$	$4.89 \times 10^{-8}$



pristine NiCoS, both the Co 2p<sub>3/2</sub> and Ni 2p<sub>3/2</sub> spectra show an obvious oxidation state (at 781.0 and 856.4 eV, respectively) originating from superficial oxidation. These surface oxidation layers could activate the surface metal sites and provide extra bonding effect for polysulfides<sup>35</sup>. Upon contact with  $Li_2S_6$ , both the Co-S and Co-O peaks shift to significantly lower binding energies (Fig. 3d), confirming the chemical interaction between NiCoS and polysulfide that results in electron transfer from  $Li_2S_6$  molecules to Co atoms<sup>36</sup>. Similarly, both the Ni-S and Ni-O peaks shift toward lower binding energy, suggesting the electron transfer from  $Li_2S_6$  molecules to Ni atoms (Fig. 3e). Both the DFT calculations and XPS analysis confirm the strong chemical adsorption of NiCoS for polysulfides.

To explore the effect of the NiCoS layer on the electrochemical reaction kinetics, in situ electrochemical impedance spectroscopy (EIS) was performed during the cycling processes based on the bare PP, NiCoS/PP and NiCoS/PP-P separators (Fig. 4). The Nyquist impedance plots in Fig. 4a–d were recorded at the potentials of open circuit voltage (OCV), 2.1 V (discharge), 1.7 V (discharge), and 2.8 V (recharge), respectively, corresponding to the a, b, c, and d points in the cyclic voltammetry (CV) curves (Fig. S11). All the EIS spectra are modeled with equivalent circuits (Fig. 4e), and the corresponding results are summarized in Table S2. As shown in Fig. 4a, all the fresh cells display only one semicircle, corresponding to the charge-

transfer resistance  $R_1$ . After introducing the NiCoS layer, the charge-transfer resistance slightly decreases (80.8  $\Omega$ ), indicating that the NiCoS thin film can facilitate charge transportation along the electrolyte/electrode interface owing to the porous and conductive nature of the NiCoS layer. With compression treatment, the charge-transfer resistance shows a negligible change (81.5  $\Omega$ ). When the cells are discharged to 2.1 V, all the EIS spectra display an additional semicircle in medium frequency, corresponding to the interface contact resistance ( $R_2$ ) between the soluble polysulfide and the cathode electrode (Fig. 4b)<sup>37</sup>. In addition, the charge-transfer resistance  $R_1$  of all the cells shows a dramatic decrease (< 54  $\Omega$ ), revealing good electrolyte infiltration into the cathode and better contact between the electrolyte and cathode. Both of the cells with NiCoS/PP and NiCoS/PP-P separators exhibit smaller  $R_1$  and  $R_2$  values than those with bare PP separators. Upon further discharge to 1.7 V, solid lithium sulfides ( $Li_2S_2/Li_2S$ ) are formed. Thus, the semicircles representing  $R_2$  increase dramatically for all the cells (Fig. 4c), demonstrating an increased lithium sulfides/cathode interface contact resistance. Since porous NiCoS nanosheet arrays can provide abundant voids to accommodate various redox species and suppress the deposition of the  $Li_2S$  layer between the cathode and separator, the cells with NiCoS/PP and NiCoS/PP-P separators exhibit much smaller  $R_2$  than those with bare PP. In addition, for all the cells, an additional semicircle ( $R_3$ ) appears between  $R_1$  and  $R_2$ ,

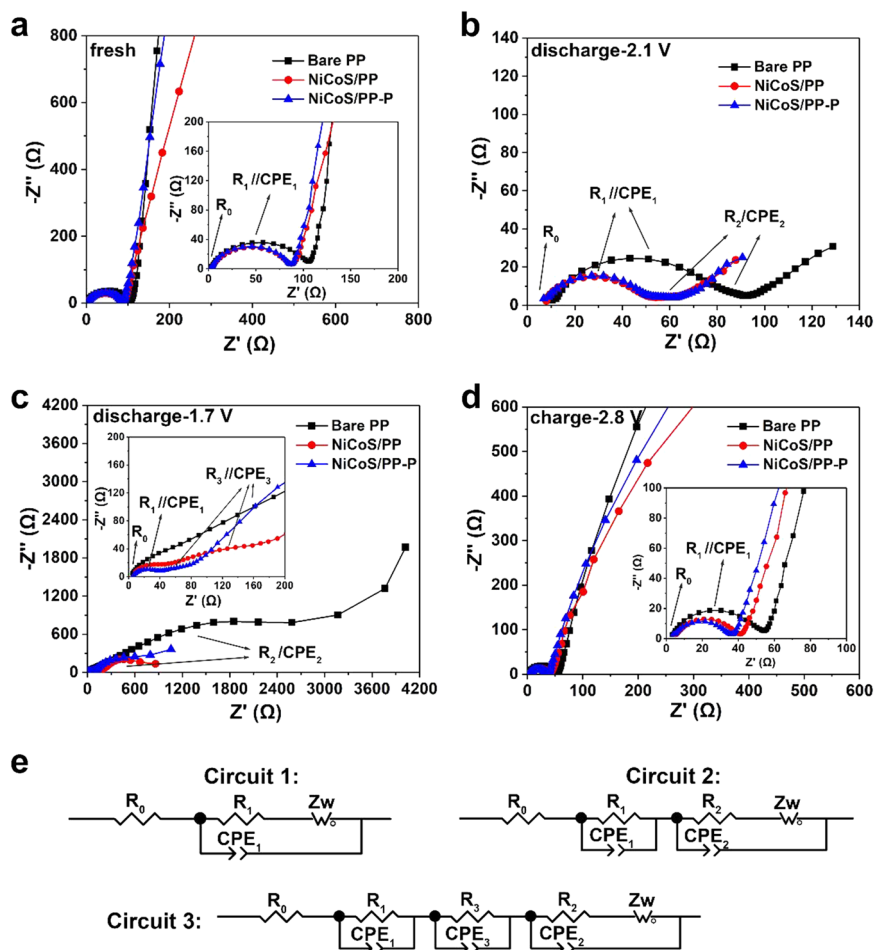
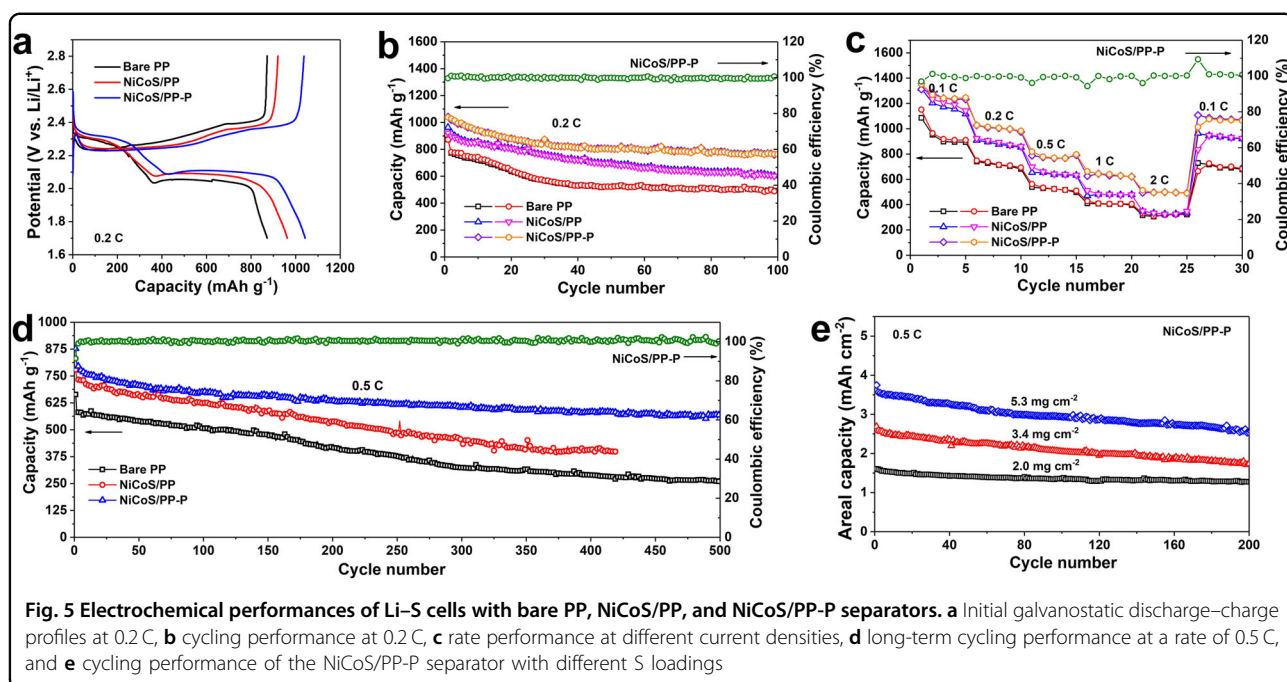


**Fig. 4** In situ EIS analysis of the Li-S cells with bare PP, NiCoS/PP, and NiCoS/PP-P separators recorded at different potentials. **a** Open circuit voltage, **b** 2.1 V in discharge, **c** 1.7 V in discharge, and **d** 2.8 V in recharge. **e** Corresponding equivalent circuits: circuit 1 represents (a), (d), circuit 2 refers to (b), and circuit 3 corresponds to (c)

representing the interface contact resistance between the diffused polysulfide and anode<sup>37</sup>. The cell with NiCoS/PP-P shows the smallest  $R_3$  (35.86  $\Omega$ ) among all the cells (see the  $R_3$  values in Table S2), revealing that the compressed NiCoS thin film significantly suppresses polysulfide migration to the anode. After recharge to 2.8 V, all the EIS spectra recover to a semicircle in the high-frequency region ( $R_1$ ) and an inclined line in the low-frequency region (Fig. 4d). The charge-transfer resistance  $R_1$  of all the cells decreases significantly in contrast to the pristine cells because the cycling processes result in improved wettability between the electrolyte and cathode. In addition, the  $R_1$  value of the NiCoS/PP-P separator is smaller than that of NiCoS/PP, indicating that the suppression of polysulfide diffusion can decrease the internal resistance in the subsequent cycles. The results also suggest that conductive NiCoS can facilitate redox reactions by forming an upper current collector between the PP membrane and cathode<sup>15</sup>.

To demonstrate the superiority of the compressed NiCoS/PP separator, the performances of Li-S batteries with bare PP, NiCoS/PP, and NiCoS/PP-P separators were evaluated, as shown in Fig. 5. The commercial CNT was chosen as the cathode host material to fabricate the CNT/S cathode. The sulfur content of the CNT/S cathode is as high as 75 wt%, and the areal sulfur loading is  $\sim 1.5\text{--}2\text{ mg cm}^{-2}$ . According to the different separators applied, the cells are denoted as bare PP, NiCoS/PP, and NiCoS/PP-P, respectively. Figure 5a compares the galvanostatic discharge-charge profiles of the three cells at a current density of 0.2 C ( $1\text{ C} = 1673\text{ mA g}^{-1}$ ). All of the profiles show two discharge plateaus and two charge plateaus. For NiCoS/PP-P, the two discharge plateaus at 2.32 and 2.11 V are assigned to the reduction of sulfur to long-chain lithium polysulfide  $\text{Li}_2\text{S}_x$  ( $4 \leq x \leq 8$ ) and the subsequent conversion to short-chain sulfides ( $\text{Li}_2\text{S}_2/\text{Li}_2\text{S}$ ), respectively<sup>38</sup>. The charge plateaus at 2.23 and 2.37 V correspond to the oxidation of  $\text{Li}_2\text{S}/\text{Li}_2\text{S}_2$  to long-chain





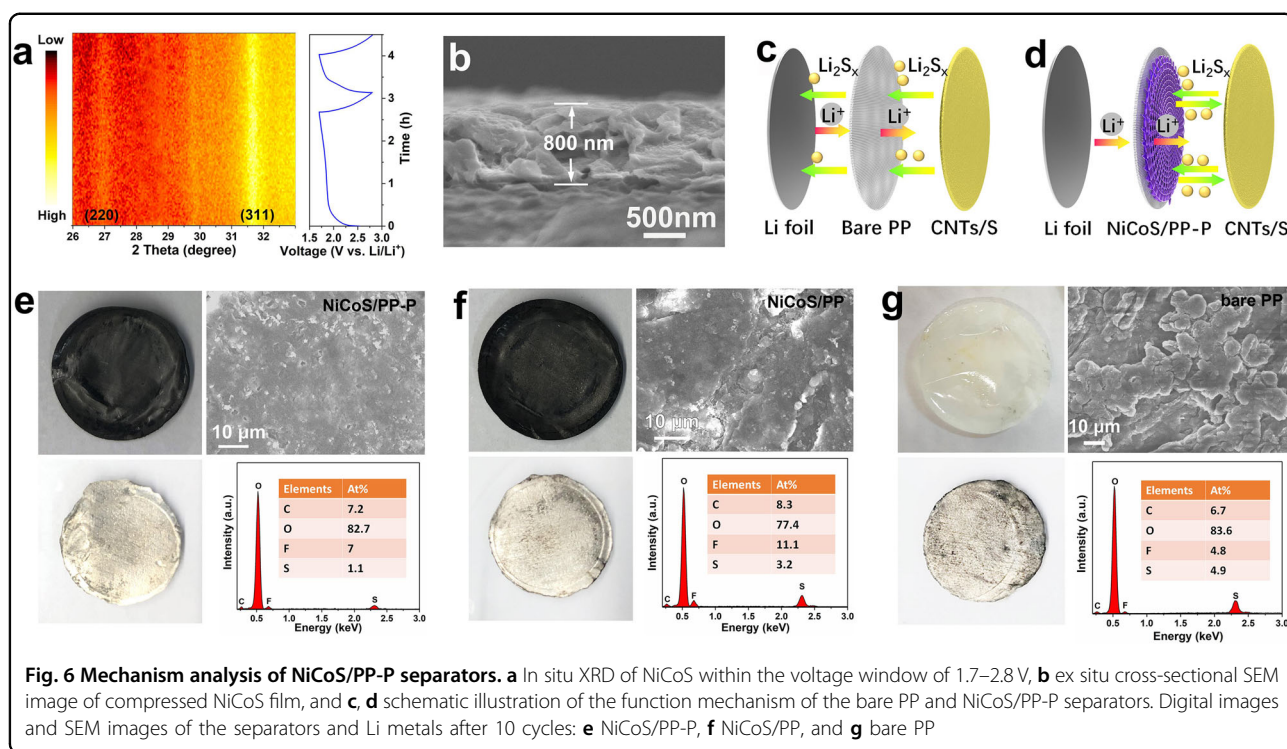
polysulfides and then to sulfur<sup>38</sup>. Compared with the bare PP and NiCoS/PP, the NiCoS/PP-P exhibits longer and flatter plateaus with lower polarization because the conductive and compressed NiCoS thin film can enhance the redox reaction kinetics and improve the sulfur utilization. As a result, NiCoS/PP-P delivers a higher discharge capacity ( $1041 \text{ mAh g}^{-1}$ ) than NiCoS/PP ( $964 \text{ mAh g}^{-1}$ ) and bare PP ( $873 \text{ mAh g}^{-1}$ ). Figure 5b compares the cycling performance of bare PP, NiCoS/PP, and NiCoS/PP-P at a current density of 0.2 C. The bare PP presents a reversible capacity of  $488 \text{ mAh g}^{-1}$  after 100 cycles, with a low capacity retention of 55.9%. After applying the compressed NiCoS/PP separator, the NiCoS/PP-P exhibits a much higher capacity of  $765 \text{ mAh g}^{-1}$  after 100 cycles, corresponding to an improved capacity retention of 74%. In addition, over the entire cycling process, the NiCoS/PP-P exhibits a high Coulombic efficiency of  $\sim 99.6\%$ . The improved capacity retention of NiCoS/PP-P implies that the compressed NiCoS layer can effectively suppress the polysulfide shuttling, in good agreement with the polysulfide diffusion measurements.

The rate capabilities of bare PP, NiCoS/PP, and NiCoS/PP-P were then evaluated at various current densities from 0.1 to 2 C (Fig. 5c). The average capacities of NiCoS/PP-P at 0.1, 0.2, 0.5, 1, and 2 C are 1231, 1004, 779, 644, and  $499 \text{ mAh g}^{-1}$ , respectively. When the current density returns to 0.1 C, the capacity recovers to a high value of  $1086 \text{ mAh g}^{-1}$ , indicating the good reversibility of NiCoS/PP-P. At various current rates, the NiCoS/PP-P always exhibits the highest capacity among the three cells, corresponding to the best reaction kinetics and highest sulfur

utilization of the NiCoS/P-P cell. Long-term cycling is further studied at a high current rate of 0.5 C (Fig. 5d). Remarkably, the NiCoS/PP-P delivers a high capacity of  $573 \text{ mAh g}^{-1}$  after 500 cycles, corresponding to a high-capacity retention of 71.5% (0.056% capacity decay per cycle), which is better than most previous works based on separator modification (see the comparison in Table S3). In contrast, the bare PP shows a much lower capacity of  $\sim 262.3 \text{ mAh g}^{-1}$  after 500 cycles. Over long-term cycling, the Coulombic efficiency of NiCoS/PP-P is maintained at  $\sim 99.6\%$ . With thin and lightweight barrier layers, the NiCoS/PP-P separator enables the commercial CNT/S cathode with excellent cycling stability and rate capability, highlighting the superiority of the NiCoS/PP-P separator for high-performance Li-S battery. To further improve the energy density of the Li-S battery system and inspect the feasibility of the NiCoS/PP-P separator, CNT/S electrodes with different areal sulfur loadings were evaluated at 0.5 C (Fig. 5e, Fig. S12). It can be noted that with a high sulfur loading up to  $5.3 \text{ mg cm}^{-2}$ , the CNT/S cathode still approaches a high reversible capacity of  $495 \text{ mAh g}^{-1}$  after 200 cycles, corresponding to a high areal capacity of  $2.63 \text{ mAh cm}^{-2}$ . This result indicates that the NiCoS/PP-P membrane can enable the Li-S battery to achieve stable cycling even with high sulfur loading.

## Discussion

Notably, NiCoS nanosheet arrays contribute a very low lithium storage capacity ( $\sim 9.6 \text{ mAh g}^{-1}$ ) in the voltage window of 1.7–2.8 V (Fig. S13), indicating that the NiCoS thin film is chemically stable for the Li-S battery. To



further confirm the chemical stability of NiCoS, in situ XRD measurements in the 1.7–2.8 voltage window were performed by using NiCo<sub>2</sub>S<sub>4</sub> as the electrode (Fig. 6a). The results reveal that over the first and second cycles, the (220) and (311) peaks from NiCo<sub>2</sub>S<sub>4</sub> (JCPDS No. 01-073-1704) do not change or shift, demonstrating the excellent chemical stability of NiCo<sub>2</sub>S<sub>4</sub> in the 1.7–2.8 voltage window.

The superior trapping performance of NiCoS/PP-P is due to the compressed NiCoS thin film that provides physical/chemical entrapment of polysulfides and facilitates the redox reactions (Fig. 6c, d). To demonstrate the functional roles of the compressed NiCoS layer upon cycling, ex situ observations of the NiCoS/PP-P, NiCoS/PP and bare PP after 10 cycles were obtained. The separators were collected from the disassembled cell without any cleaning. As shown in Fig. 6e–g, the cycled NiCoS/PP and bare PP (top left) show obvious grayish yellow residues, corresponding to the polysulfide species. For NiCoS/PP-P, only some inconspicuous gray residues are observed, indicating that most of the dissolved polysulfides have been converted to solid sulfur during the recharge process. The corresponding top-view SEM image (Fig. S14) shows that a solid porous layer covers the compressed NiCoS nanosheet arrays, which can be ascribed to the electrolyte residue or solid electrolyte interface layer<sup>39</sup>. The cross-sectional SEM images of the compressed NiCoS films (Fig. 6b) reveal that the NiCoS layer preserves its nanosheet array structure with an

unchanged thickness of 800 nm, and no crack or pulverization can be observed, suggesting the robust adhesion of the NiCoS layer on the PP membrane. Furthermore, the cycled Li metals were studied, as shown in Fig. 6e–g (bottom left). Compared with Li metal with bare PP and NiCoS/PP separators, Li metal with a NiCoS/PP-P separator is shinier and cleaner, indicating that the NiCoS/PP-P efficiently suppresses the polysulfide diffusion to the Li-metal anode. The corresponding morphologies (Fig. 6e–g, top right) reveal that the Li-metal surface with the NiCoS/PP-P separator is relatively smooth, demonstrating that the compressed NiCoS/PP membrane suppresses Li dendrite formation, possibly due to the synergetic effect of lithium polysulfide and lithium nitrate that can form a stable and uniform solid electrolyte interphase layer on the Li-metal surface<sup>40</sup>. The bare PP shows obvious Li dendrite due to the serious corrosion of Li metal by lithium polysulfides, which leads to inhomogeneous Li<sup>+</sup> flux and formation of a Li dendrite. The elemental analysis of Li metal (Fig. 6e–g, bottom right) reveals that Li metal with compressed NiCoS/PP was determined to have the lowest sulfur content, further confirming that the NiCoS/PP-P separator successfully alleviates polysulfide shuttling. The superior trapping performance of NiCoS/PP-P can be ascribed to the following reasons: (i) the hierarchical porous NiCoS nanosheet arrays can provide abundant chemical bonding sites to anchor the polysulfides; (ii) the compressed NiCoS thin film has a compacted structure to prevent polysulfide

diffusion; (iii) several layers of bending nanosheets covering the NiCoS surface block the open pores and alleviate polysulfide migration; (iv) the conductive and porous NiCoS layer can help reactive the dead sulfur species in the separator and facilitate redox reactions by forming an upper current collector between the PP membrane and cathode.

In summary, we have developed a multifunctional separator for use in long-life Li–S batteries by growing conductive and lightweight NiCoS ( $\text{NiCo}_2\text{S}_4$ ) nanosheet arrays on one side of a commercial PP membrane. In contrast to traditional vacuum-filtration and slurry-coating methods, the in situ growth strategy results in a uniform NiCoS thin film tightly adhering to the PP membrane without any binder. The uniform conductive NiCoS layer is thin ( $0.8\ \mu\text{m}$ ) and lightweight ( $0.148\ \text{mg cm}^{-2}$ ), which has little effect on the gravimetric/volumetric energy densities of the Li–S battery. More importantly, porous and conductive compressed NiCoS nanosheet arrays not only physically inhibit polysulfide migration and chemically anchor polysulfides but also provide a continuous electron transport pathway and facilitate fast  $\text{Li}^+$  transportation. Thus, the compressed NiCoS-modified separator endows the sulfur cathode made of commercial CNT and sulfur with a high Coulombic efficiency ( $\sim 99.6\%$  at  $0.2\ \text{C}$ ), a long cycle life (500 cycles with  $0.056\%$  capacity decay per cycle) and excellent rate performance. The in situ growth strategy combined with the mechanical compression method demonstrated in this work provides a new perspective for fabricating multifunctional separators for high-performance Li–S batteries.

#### Acknowledgements

This research is supported by the National Research Foundation, Prime Minister's Office, Singapore, under its NRF-ANR Joint Grant Call (NRF-ANR Award No. NRF2015-NRF-ANR000-CEENEMA). Wang Ye acknowledges the support from the National Natural Science Foundation of China (Grant Nos. 21603192 and U1804132).

#### Author details

<sup>1</sup>Pillar of Engineering Product Development, Singapore University of Technology and Design, 8 Somapah Road, 487372 Singapore, Singapore. <sup>2</sup>Hubei Key Laboratory of Catalysis and Materials Science, South-Central University for Nationalities, Wuhan, Hubei 430074, China. <sup>3</sup>Key Laboratory of Material Physics of Ministry of Education, School of Physics and Engineering, Zhengzhou University, Zhengzhou 450052, China. <sup>4</sup>Department of Materials Science and Engineering, National University of Singapore, 117574 Singapore, Singapore. <sup>5</sup>Beijing Key Laboratory of Electrochemical Process and Technology for Materials, Beijing University of Chemical, Technology, Beijing 100029, P. R. China

#### Author contributions

S.Z.H. and H.Y.Y. conceived the idea and designed the experiments, analyzed the results, and wrote the paper. Y.W. prepared the sample and measured the in situ XRD. J.H. performed the DFT calculation. Y.V.L. and D.K. conducted the battery performance measurements. L.G. performed the XRD and BET measurements. Z.K. performed the TEM. Y.C. contributed to discussions and interpretation of results.

#### Conflict of interest

The authors declare that they have no conflict of interest.

#### Publisher's note

Springer Nature remains neutral with regard to jurisdictional claims in published maps and institutional affiliations.

**Supplementary Information** is available for this paper at <https://doi.org/10.1038/s41427-019-0159-1>.

Received: 1 April 2019 Revised: 15 July 2019 Accepted: 16 July 2019  
Published online: 11 October 2019

#### References

- Armand, M. & Tarascon, J.-M. Building better batteries. *Nature* **451**, 652 (2008).
- Huang, S. et al. Rationally engineered amorphous  $\text{TiO}_x/\text{Si}/\text{TiO}_x$  nanomembrane as an anode material for high energy lithium ion battery. *Energy Storage Mater.* **12**, 23–29 (2018).
- Scrosati, B., Hassoun, J. & Sun, Y.-K. Lithium-ion batteries. A look into the future. *Energy Environ. Sci.* **4**, 3287–3295 (2011).
- Peng, H.-J., Huang, J.-Q. & Zhang, Q. A review of flexible lithium–sulfur and analogous alkali metal–chalcogen rechargeable batteries. *Chem. Soc. Rev.* **46**, 5237–5288 (2017).
- Seh, Z. W., Sun, Y., Zhang, Q. & Cui, Y. Designing high-energy lithium–sulfur batteries. *Chem. Soc. Rev.* **45**, 5605–5634 (2016).
- Chen, W. et al. A new hydrophilic binder enabling strongly anchoring polysulfides for high-performance sulfur electrodes in lithium–sulfur battery. *Adv. Energy Mater.* **8**, 1702889 (2018).
- Zhao, Q. et al. Three-dimensional carbon current collector promises small sulfur molecule cathode with high areal loading for lithium–sulfur batteries. *ACS Appl. Mater. Interfaces* **10**, 10882–10889 (2018).
- Abbas, S. A. et al. Modified separator performing dual physical/chemical roles to inhibit polysulfide shuttle resulting in ultrastable Li–S batteries. *ACS Nano* **11**, 12436–12445 (2017).
- Sahore, R. et al. Design principles for optimum performance of porous carbons in lithium–sulfur batteries. *Adv. Energy Mater.* **6**, 1600134 (2016).
- Zhu, Q. et al. Ultra-microporous carbons encapsulate small sulfur molecules for high performance lithium–sulfur battery. *Nano Energy* **33**, 402–409 (2017).
- Mi, K. et al. Sole chemical confinement of polysulfides on nonporous nitrogen/oxygen dual-doped carbon at the kilogram scale for lithium–sulfur batteries. *Adv. Funct. Mater.* **27**, 1604265 (2017).
- Huang, S. et al. Regulating the polysulfide redox conversion by iron phosphide nanocrystals for high-rate and ultrastable lithium–sulfur battery. *Nano Energy* **51**, 340–348 (2018).
- Zhao, Q., Zhu, Q., Miao, J., Zhang, P. & Xu, B. 2D MXene nanosheets enable small-sulfur electrodes to be flexible for lithium–sulfur batteries. *Nanoscale* **11**, 8442–8448 (2019).
- Ghazi, Z. A. et al.  $\text{MoS}_2/\text{celgard}$  separator as efficient polysulfide barrier for long-life lithium–sulfur batteries. *Adv. Mater.* **29**, 1606817 (2017).
- Huang, J.-Q., Zhang, Q. & Wei, F. Multi-functional separator/interlayer system for high-stable lithium–sulfur batteries: progress and prospects. *Energy Storage Mater.* **1**, 127–145 (2015).
- Pei, F. et al. A two-dimensional porous carbon-modified separator for high-energy-density Li–S batteries. *Joule* **2**, 323–336 (2017).
- Yao, H. et al. Improved lithium–sulfur batteries with a conductive coating on the separator to prevent the accumulation of inactive S-related species at the cathode–separator interface. *Energy Environ. Sci.* **7**, 3381–3390 (2014).
- Zhou, T. et al. Twinborn  $\text{TiO}_2\text{–TiN}$  heterostructures enabling smooth trapping–diffusion–conversion of polysulfides towards ultralong life lithium–sulfur batteries. *Energy Environ. Sci.* **10**, 1694–1703 (2017).
- Bai, S., Liu, X., Zhu, K., Wu, S. & Zhou, H. Metal–organic framework-based separator for lithium–sulfur batteries. *Nat. Energy* **1**, 16094 (2016).
- Jeong, Y. C., Kim, J. H., Nam, S., Park, C. R. & Yang, S. J. Rational design of nanostructured functional interlayer/separator for advanced Li–S batteries. *Adv. Funct. Mater.* **28**, 1707411 (2018).
- Xiao, J., Wan, L., Yang, S., Xiao, F. & Wang, S. Design hierarchical electrodes with highly conductive  $\text{NiCo}_2\text{S}_4$  nanotube arrays grown on carbon fiber paper for high-performance pseudocapacitors. *Nano Lett.* **14**, 831–838 (2014).



22. Xia, C., Li, P., Gandi, A. N., Schwingenschlöggl, U. & Alshareef, H. N. Is NiCo<sub>2</sub>S<sub>4</sub> really a semiconductor? *Chem. Mater.* **27**, 6482–6485 (2015).
23. Perdew, J. P., Burke, K. & Ernzerhof, M. Generalized gradient approximation made simple. *Phys. Rev. Lett.* **77**, 3865 (1996).
24. Kresse, G. & Furthmüller, J. Self-interaction correction to density functional approximation for many electron systems. *Phys. Rev. B* **54**, 11169 (1996).
25. Wang, L., Maxisch, T. & Ceder, G. Oxidation energies of transition metal oxides within the GGA+U framework. *Phys. Rev. B* **73**, 195107 (2006).
26. Monkhorst, H. J. & Pack, J. D. Special points for Brillouin-zone integrations. *Phys. Rev. B* **13**, 5188 (1976).
27. Vayssieres, L., Beermann, N., Lindquist, S.-E. & Hagfeldt, A. Controlled aqueous chemical growth of oriented three-dimensional crystalline nanorod arrays: application to iron (III) oxides. *Chem. Mater.* **13**, 233–235 (2001).
28. Liu, Z., Fan, T. & Zhang, D. Synthesis of biomorphous nickel oxide from a pinewood template and investigation on a hierarchical porous structure. *J. Am. Ceram. Soc.* **89**, 662–665 (2006).
29. Zhou, G. et al. A flexible sulfur-graphene-polypropylene separator integrated electrode for advanced Li–S batteries. *Adv. Mater.* **27**, 641–647 (2015).
30. Dong, Y. et al. All-MXene-based integrated electrode constructed by Ti<sub>3</sub>C<sub>2</sub> nanoribbon framework host and nanosheet interlayer for high-energy-density Li–S batteries. *ACS Nano* **12**, 2381–2388 (2018).
31. Huang, J.-Q. et al. Permselective graphene oxide membrane for highly stable and anti-self-discharge lithium–sulfur batteries. *ACS Nano* **9**, 3002–3011 (2015).
32. Zhou, G. in *Design, Fabrication and Electrochemical Performance of Nanostructured Carbon Based Materials for High-Energy Lithium–Sulfur Batteries* 75–94 (Springer, 2017).
33. He, J., Luo, L., Chen, Y. & Manthiram, A. Yolk-shelled C@Fe<sub>3</sub>O<sub>4</sub> nanoboxes as efficient sulfur hosts for high-performance lithium–sulfur batteries. *Adv. Mater.* **29**, 1702707 (2017).
34. Liang, X. et al. A highly efficient polysulfide mediator for lithium–sulfur batteries. *Nat. Commun.* **6**, 5682 (2015).
35. Zhong, Y. et al. Surface chemistry in cobalt phosphide-stabilized lithium-sulfur batteries. *J. Am. Chem. Soc.* **140**, 1455–1459 (2018).
36. Pang, Q., Kundu, D. & Nazar, L. F. A graphene-like metallic cathode host for long-life and high-loading lithium–sulfur batteries. *Mater. Horiz.* **3**, 130–136 (2016).
37. Sun, J. et al. Entrapment of polysulfides by a black-phosphorus-modified separator for lithium–sulfur batteries. *Adv. Mater.* **28**, 9797–9803 (2016).
38. Huang, S. et al. Mechanism investigation of high-performance Li-polysulfide batteries enabled by tungsten disulfide nanopetals. *ACS Nano* **12**, 9504–9512 (2018).
39. Manthiram, A., Yu, X. & Wang, S. Lithium battery chemistries enabled by solid-state electrolytes. *Nat. Rev. Mater.* **2**, 16103 (2017).
40. Li, W. et al. The synergetic effect of lithium polysulfide and lithium nitrate to prevent lithium dendrite growth. *Nat. Commun.* **6**, 7436 (2015).